

Article

The 2022 Mw 6.1 Pasaman Barat, Indonesia Earthquake, Confirmed the Existence of the Talamau Segment Fault Based on Teleseismic and Satellite Gravity Data

Bondan Galih Dewanto ^{1,2,3} , Ramadhan Priadi ⁴, Leni Sophia Heliani ^{1,3,*}, Al Shida Natul ⁵, Muhammad Yanis ⁶ , Indranova Suhendro ^{2,7} and Admiral Musa Julius ⁸

- ¹ Department of Geodetic Engineering, Universitas Gadjah Mada, Jl. Grafika No.2 Bulaksumur, Yogyakarta 55281, Indonesia
 - ² Center for Disaster Studies, Universitas Gadjah Mada, Yogyakarta 55281, Indonesia
 - ³ Hazard and Risk Management Center of Excellent, Faculty of Engineering, Universitas Gadjah Mada, Yogyakarta 55281, Indonesia
 - ⁴ Gowa Geophysical Station, Agency for Meteorology Climatology and Geophysics (BMKG), Jl. Poros Malino, Sungguminasa 92112, Indonesia
 - ⁵ Master Program in Geomatics Engineering, Department of Geodetic Engineering, Universitas Gadjah Mada, Jl. Grafika No.2 Bulaksumur, Yogyakarta 55281, Indonesia
 - ⁶ Geophysical Engineering Department, Universitas Syiah Kuala, Banda Aceh 23111, Indonesia
 - ⁷ Department of Environmental Geography, Faculty of Geography, Universitas Gadjah Mada, Sekip Utara Jl. Kaliurang, Bulaksumur, Yogyakarta 55281, Indonesia
 - ⁸ Earthquake and Tsunami Center, Agency for Meteorology Climatology and Geophysics (BMKG), Jl. Angkasa 1 No.2, Kemayoran, Jakarta 10610, Indonesia
- * Correspondence: lheliani@ugm.ac.id



Citation: Dewanto, B.G.; Priadi, R.; Heliani, L.S.; Natul, A.S.; Yanis, M.; Suhendro, I.; Julius, A.M. The 2022 Mw 6.1 Pasaman Barat, Indonesia Earthquake, Confirmed the Existence of the Talamau Segment Fault Based on Teleseismic and Satellite Gravity Data. *Quaternary* **2022**, *5*, 45. <https://doi.org/10.3390/quat5040045>

Academic Editor: Jef Vandenberghe

Received: 13 July 2022

Accepted: 15 October 2022

Published: 2 November 2022

Publisher's Note: MDPI stays neutral with regard to jurisdictional claims in published maps and institutional affiliations.



Copyright: © 2022 by the authors. Licensee MDPI, Basel, Switzerland. This article is an open access article distributed under the terms and conditions of the Creative Commons Attribution (CC BY) license (<https://creativecommons.org/licenses/by/4.0/>).

Abstract: A Mw 6.1 earthquake on 25 February 2022, at around 8:39 a.m. local time, struck Pasaman Barat Regency, West Sumatra, Indonesia, and was felt in Singapore and Malaysia. The hypocenter of this earthquake was 12 km deep and preceded by an Mw 4.9 foreshock a few minutes earlier. The earthquakes originated on a blind fault and triggered a landslide at Mount Talamau. Herein, the slip distribution and asperities along the plane fault during the earthquake were examined by teleseismic inversion and the fault location was identified by Global Gravity Model plus (GGMplus) satellite gravity data. The slip distribution was calculated from the source parameters (strike: 136°; dip: 70°; rake: 174°) by inversion techniques based on teleseismic data. Based on the slip distribution, the earthquake was generated by stress from the Sianok fault that spread to the north and reached the uncertain fault segment in the Talamau area. In addition, the results of the First Horizontal Derivative and Second Vertical Derivative from the GGMplus data revealed a straight Simple Bouguer Anomaly pattern, confirming the existence of the uncertain Talamau fault as part of the Great Sumatra Fault. This work shows the potential application of the combination of teleseismic and gravity observation for delineating the fault structure that caused the 2022 Mw 6.1 Pasaman earthquake, which can also be applied to other locations of similar geological backgrounds.

Keywords: Pasaman earthquake; teleseismic; satellite gravity; Sumatra Fault Zone

1. Introduction

Sumatra Island, Indonesia, is a geologically complex region that includes the Great Sumatra Fault (GSF) in the middle of the island, the Mentawai Fault Zone between Sumatra Island and the Mentawai Islands, and a subduction zone created by the interaction of the Eurasian continental and Indo-Australian Ocean plates. The GSF is a ±1650 km-long strike-slip fault, running along from Banda Aceh to Semangko Bay, which lies above the subduction between Eurasian and Indo-Australian plates [1,2]. Such highly active subduction on the western side (52–60 mm/y) combined with an intense spreading activity

of the Andaman Sea on the northern side (38 mm/y) are, therefore, responsible for the formation of 19 fault segments along the GSF and causing the GSF to move in a dextral fashion at varying rates, 23–27, 11–23, and 6.8–11 mm/y for the north, middle, and south segments of Sumatra Island, respectively (Figure 1) [3,4]. The intense movement of the GSF is, therefore, responsible for the formation of ± 13 pull-apart basins along the GSF [5], as the length of each fault segment increases as fault displacement decreases under an extensional regime [6]. As a consequence, earthquakes become the most significant threats along the GSF. More than a dozen earthquakes have occurred along the GSF over the past 200 years [7]. Seven of 19 segments in the GSF are located in West Sumatra Province [8], namely, Siulak (2.25–1.7° S), Suliti (1.75–1.0° S), Sumani (1.0–0.5° S), Sianok (0.7° S–0.1° N), Sumpur (0.1–0.3° N), Barumun (0.3–1.2° N), and Angkola (0.3–1.2° N). In addition, many densely populated settlements have been built around the West Sumatra segments (i.e., Padang sidempuan, Bukittinggi, Solok), making the vulnerability high [7].

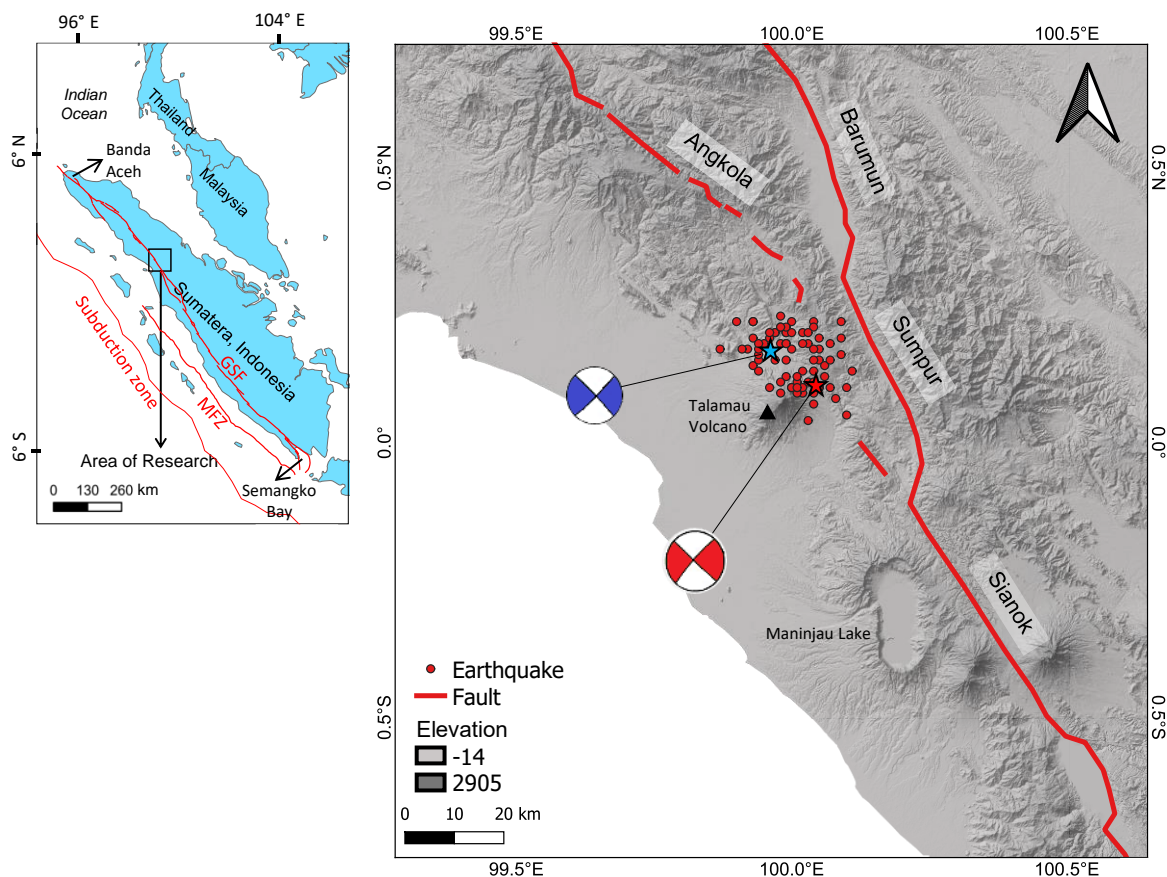


Figure 1. Study area and earthquake location map. White–blue and white–red beach balls show the earthquake that occurred at 08:35 and 08:39 local time, respectively, while the blue and red stars are the epicenter locations. The black triangle is the location of Talamau Volcano.

On 25 February 2022, the Pasaman earthquake ($M_w = 6.1$) caused landslides around the vicinity of Talamau Volcano (Figure 2), claiming 27 lives and destroying 6627 houses. This event was preceded by an $M_w 4.9$ foreshock and ended with 201 aftershocks that were felt until 4 March 2022. From the seismic activities, BMKG stated that the source of the earthquake was triggered by the movement of a possible new Talamau fault segment, confirmed by the geological map to be an uncertain fault [9]. Hence, the cause of the major earthquake that struck Pasaman is still unknown.



© Doc. of field observation 1 March 2022

Figure 2. Damage of the Pasaman earthquake: (a) landslide, (b) road damage, and (c,d) building structural damage.

Geodetic and geophysical data have been widely used to understand earthquake and crustal deformation characteristics [10–15]. The source mechanism is one of the geophysical methods for understanding the causes of earthquakes. Rupture mechanism analyses applying teleseismic body waves are widely used to get temporal and spatial variations within coseismic slip patterns. Classical teleseismic body wave inversion that uses the global wideband seismic network can be analyzed immediately after significant earthquakes [16]. On the other hand, as a geodetic method, gravity data can be gathered by the satellite technique [17–20]. The gravity method, notably with the Global Gravity Model plus (GGMPlus) data [20–22], is a high accuracy, promising, quick, economical, and simple methodology to identify the fault structure distribution [23–25], as applied to pinpoint the GSF in Aceh Province [26].

A few studies on the 2022 Pasaman earthquake have been published, including Julius et al. (2022) [27] and Kardo et al. (2022) [28]; however, they focused on the report of field observation and trauma healing for the victims. In addition to that, in Pasaman City, comprehensive fault distribution maps are not yet available to decrease hazard risks. Hence, there is still a lack of understanding of the activities of the Talamau segment and its role in the 2022 Pasaman earthquake. In this contribution, we combine teleseismic and satellite gravity data with the aim of better understanding the coseismic source model of the 2022 Mw 6.1 Pasaman earthquake and its fault structure.

2. Study Area

2.1. Focus of Study Area

Pasaman City is a regency in West Sumatra, Indonesia, situated between the latitudes of 00°33' N and 00°11' S and the longitudes of 99°10' and 100°04' E (Figure 1). The regency has diverse topography such as flat, wavy, hilly, and mountainous terrain ranges between 0 and 2912 m above sea level [29]. The topographical conditions of Pasaman City are as follows: (1) “coastal land/flat land” that extends from the tidal line to the mainland on a slope of 0–3% at 5 m above sea level (the Sasak, Muara Bingung, and Air

Bangis localities and other communities along the coast are made up of coastal alluvial deposits that produce lowlands and muddy swamps), (2) “low land” with undulating land elevations more significant than 15 m above sea level and a 3–8% slope to the foothills free of tidal zones, (3) “middle land” that is an undulating territory extending from the highest point of low land to a hilly area with a height of 50 feet above sea level and a slope of 8–15%, and (4) “upland” refers to hilly terrain with a maximum elevation of 2912 m above sea level, the majority of which are protected areas [30].

2.2. Geological Setting

The subduction in Sumatra has continued since the Late Jurassic (± 160 Ma) [31]. In such a time, numerous collisions between continental blocks occurred, including the East Malaya, Sibumasu, East Sumatra, West Sumatra, and Woyla Nappe blocks, which mainly include granitic intrusions, basaltic–andesitic volcanic rocks, volcanoclastic sedimentary rocks, limestones, and high-grade and low-grade metamorphic rocks [32] (Figure 3). Meanwhile, the spreading of the Andaman ridge is considerably young; the Andaman Sea began to spread in the late Miocene (± 10 Ma) when India and Asia were about to collide (see Figures 35 and 36 in Hall 2012). Coincidentally, the GSF has started to develop since the Pliocene (± 4 Ma onward) [33], implying that the origin of the GSF may be related to the presence of the Andaman spreading center, as well as the subduction. Since then, there has been a rapid increase in volcanic intensity in Sumatra [33], as indicated by the dense volcano distribution [34] and the occurrence of significant caldera-forming eruptions such as the 840 ka Oldest Toba Tuff, 500 ka Middle Toba Tuff, and 74 ka Youngest Toba Tuff eruptions (erupted volumes are estimated to be approximately 500–2300, 60, and 2800–5300 km³, respectively; volcano explosivity index (VEI) 8), the 52 ka Maninjau eruption (220–250 km³, VEI 7), and the 33 ka Ranau eruption (>100 km³, VEI 7) [35–40]. It is interesting that most of the Quaternary volcanism in Sumatra occurs inside and adjacent (<10 km distance) to the GSF, including the Talamau Volcano (Figure 1). However, Acocella et al. (2018) suggested a weak relationship between tectonism and magmatism in Sumatra. That is, the presence of Sumatran volcanoes is not controlled by the GSF activity, but is more controlled by slab depth, as partial melting dominantly occurs at ± 130 km slab depth [4]. The GSF tends to control the formation of pull-apart basins [5].

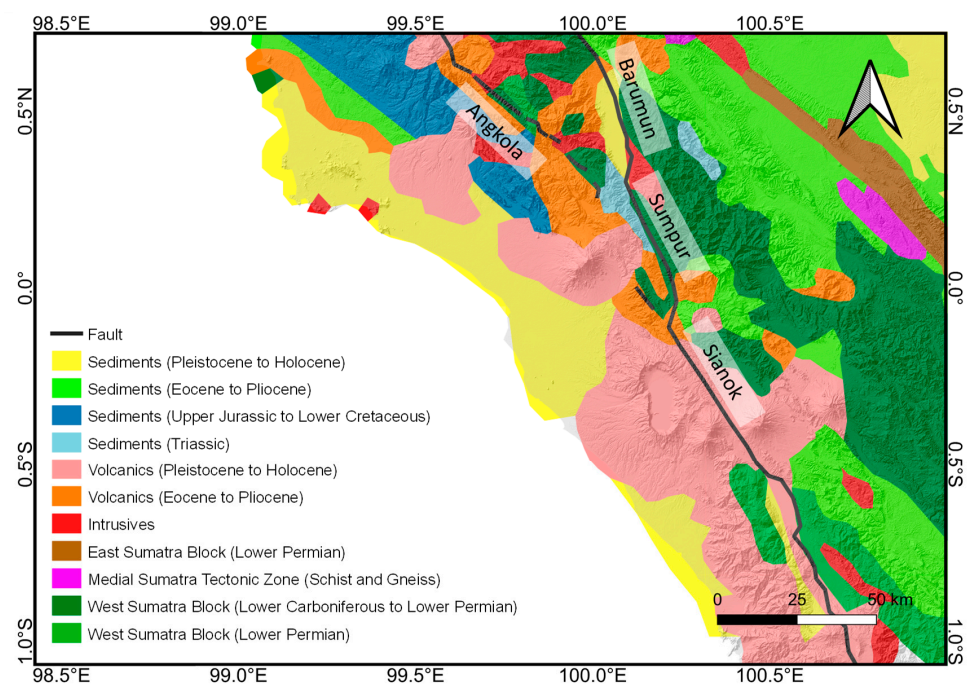


Figure 3. Geological map of Pasaman (Indonesia Geological Agency).

The Pasaman area is constructed by a complex variation of rocks [9,41] (Figure 3). This area is crossed by the Central Sumatra Fault Zone (consisting of Barumun, Angkola, Sumpur, Sianok, Sumani, Suliti, and Siulak segments) as part of the GSF (Figure 4). Particularly, the oldest stage (Permian–Cretaceous) is represented by intrusive and metamorphic rocks (from diorite to granite and low-grade to high-grade, respectively). The middle stage (Eocene–Pliocene) predominantly consists of intrusive (i.e., harzburgite, pyroxenite, dunite, diorite, granite) and volcanic rocks (i.e., lava and pyroclastic deposits), volcanoclastic and pelagic sedimentary rocks (i.e., breccia, sandstone, shale stone), and limestones. The youngest stage (Pleistocene–Holocene) mainly includes alluvial and volcanic deposits (from basaltic andesite to rhyolite), originating from the Talamau, Malintang, and Sorikmarapi Volcanoes. Most of these rocks are cut by (at least) three fault segments of the GSF, namely, the Angkola, Barumun, and Sumpur segments. By contrast, there has been no report on fault segments around the vicinity of the Talamau Volcano.

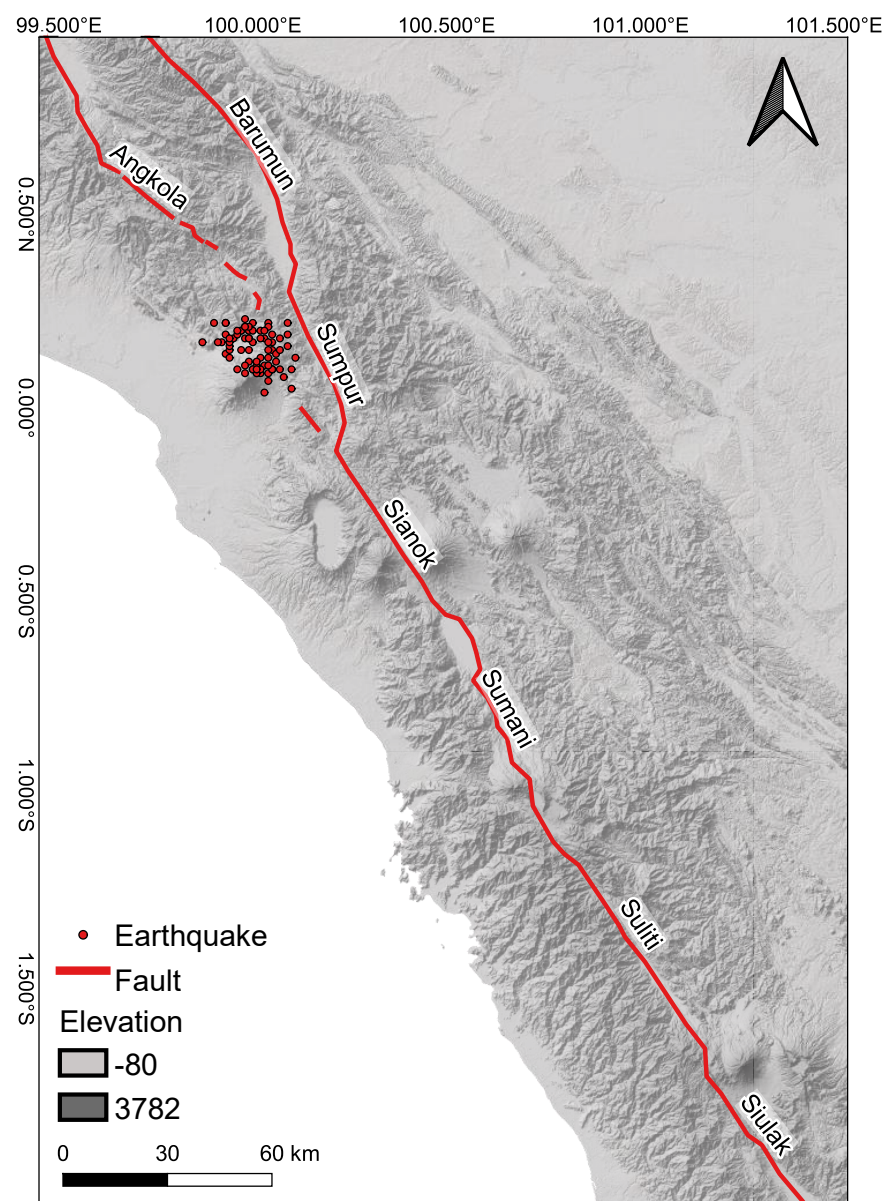


Figure 4. Central Sumatra Fault Zone. The 2022 Pasaman earthquake took place in an area where the existence of the fault is still uncertain.

3. Materials and Methods

3.1. Teleseismic Data

The displacement field observed around the fault is heavily impacted by the dimensional and temporal patterns of earthquake moment release. Seismologists have been able to depict the time-space genesis of earthquake ruptures documented by neighboring detectors in astonishing detail [42,43]. Long-period teleseismic body waves that exhibit complex waveforms can be used for understanding the displacement field near the fault [44]. Pacheo et al. (1989) [45] investigated the features of the sourcing process in the 1988 Armenian earthquake using wideband and long-duration teleseismic records. We used a developed multiple-event deconvolution technique to examine teleseismic body waves due to source variety that may have an immense impact on the dangerous power of an earthquake and the nature of coseismic deformation in a diverse tectonic context. We used teleseismic wave data to look deeper at the rupture process of the 2022 Mw 6.1 Pasaman earthquake, which started with an M4.9 foreshock followed by 201 aftershocks (Figure 5). The Data Management Center of the Incorporated Research Institutions for Seismology (IRIS) was used to connect 54 broadband stations in the Global Seismographic Network and the Federation of Digital Seismograph Networks. As far as azimuthal exposure is concerned, the observatories' epicentral distances are between 30° and 90° kilometers (Figure 6).

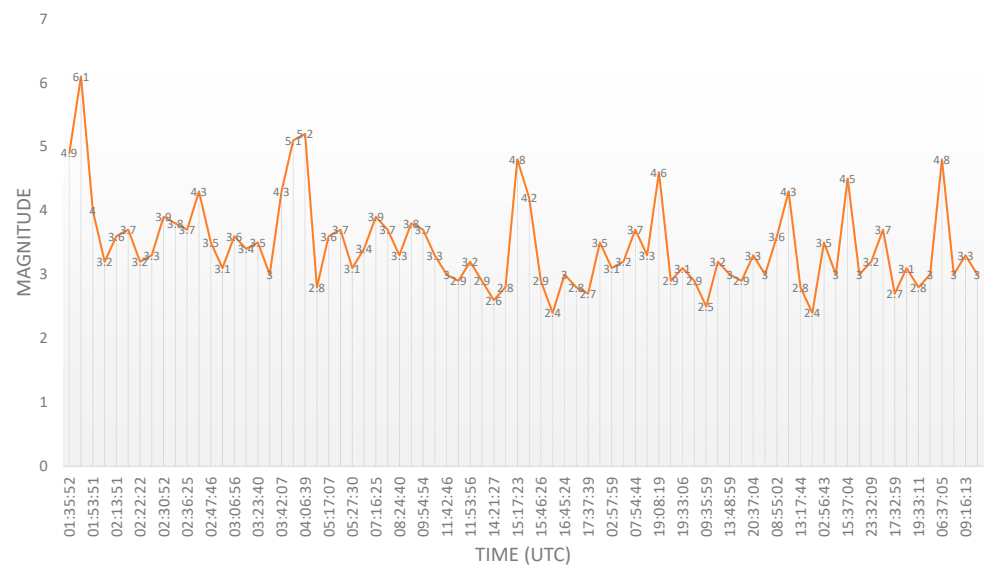


Figure 5. Earthquake activity during the Pasaman event. The main event was preceded by a magnitude 4.9 foreshock followed by 201 aftershocks.

The P and SH wave arrival times were obtained using the Jeffreys–Bullen (1958) [46] travel time chart. The start periods were adjusted within several seconds to account for lateral inhomogeneities in Earth’s travel times. At all seismic stations used, power spectral calculations were performed [44]. Afterward, the attenuation difference between the phases of the P wave and SH wave is multiplied by the factor

$$\exp \left[2\pi f \left(t_s^* - t_p^* \right) \right] \tag{1}$$

in this factor, where t_s^* and t_p^* are the attenuation constants for the P and S waves, respectively. There are several parameter criteria used for the calculation of the waveform inversion. These parameters include a clear P wave phase with minimal noise, station selection between 300 and 900 from the earthquake, and there is no data gap in the waveform.

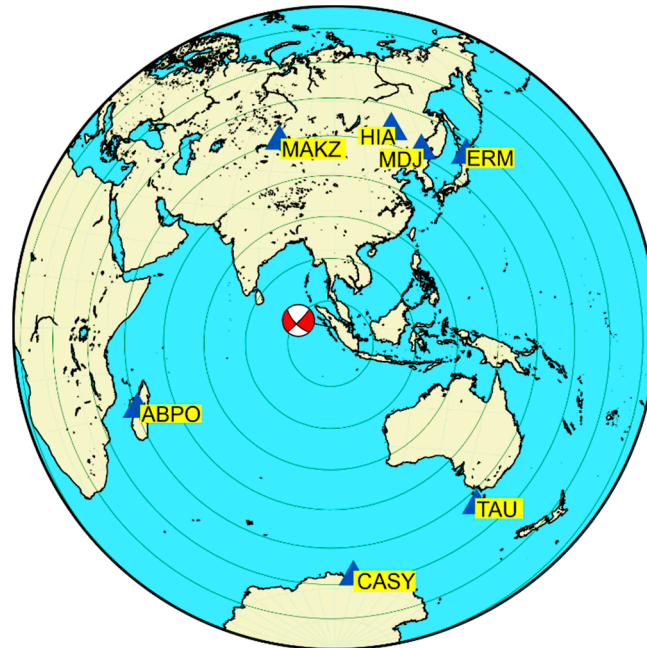


Figure 6. The selected station was used in the inversion. The green circle represents epicenter distances between 30° and 90° from the Mw 6.1 Pasaman earthquake. The red-white beach ball shows the earthquake location and the fault type as the earthquake source.

In Green’s functions, source and receiver functions were computed using Haskell’s propagator matrix [47–49]. The fault plane is assumed to have a temporal and spatial distribution of slip in each direction of each fault plane, which is spatially extended by

$$\Delta \hat{u}_i(x, t) = \sum_{j=1}^J p^j \hat{u}_t^j(t) \varnothing^j(x) f^j(x, t) \tag{2}$$

where the unit vector describing the slip direction is denoted by $\hat{u}_t^j(t)$, the slip direction is always parallel to the fault plane and is a function of time, $\varnothing^j(x)$ is a function of the spatial basis, and $f^j(x, t)$ is a function of slip time. Integrating Equation (2) for $t = \infty$ gives the final slip distribution to be

$$\Delta \hat{u}_i(x) = \sum_{j=1}^J p^j \hat{u}_t^j \varnothing^j(x) \tag{3}$$

$$\hat{u}_t^j = v_i^1 \cos \Theta^j + v_i^2 \sin \Theta^j \tag{4}$$

the notation \hat{u}_t^j indicates the rake direction in the final slip distribution, described in Equation (2). The fault plane uses two perpendicular vector units to determine the final slip distribution, namely, v_i^1 and v_i^2 . The rake angle is denoted as Θ^j measured from v_i^1 and v_i^2 . The slip distribution is determined based on T_0 (start time) and T_{st} (rupture start time). T_0 determines the initial data used for inversion, while T_{st} determines the start of rupture. The start time of the data to be used is selected at $-T_0$ a few seconds before the arrival time of the P wave.

3.2. Satellite Gravity Data

The gravitational field and fluctuations underneath and beyond Earth’s surface are detected by gravity sensors acquired from watercraft, boreholes, aircraft, and spacecraft as a combination of time and location [50,51]. Presently, the gravity anomaly of a region is commonly acquired by gravity measurements from satellites [52]. In 2000, gravity satellite missions were launched and focused on gathering data on a wide range, with a high spatial resolution and a large observation area. The Geodetic Satellite (GeoSat) by US Navy [53], European Remote Sensing (ERS) from European Space Agency (ESA), Gravity Recovery

and Climate Experiment (GRACE) from collaboration of US and German Space Agencies (NASA and DLR) [54], and Gravity Field and Steady-State Ocean Circulation Explorer (GOCE) by ESA [55] are altimetry and gravity satellites for deriving gravity information.

Herein, we used the GOCE, GGMplus, and SGG-UGM-2 data, which cover the study area of latitude -2.1° to 0.2° and longitude 119.5° to 120.5° . GGMplus [20] is a global gravity model with a spatial resolution of 200 m/px developed by combining GRACE, GOCE, SRTM, EGM 2008, and terrestrial measurement. SGG-UGM-2 is another global gravity model that combines satellite gravimetry, satellite altimetry, and Earth Gravitational Model 2008 (EGM2008). In this gravity method, the Simple Bouguer Anomaly (SBA) was used, as its value indicates the distribution of geological rocks and geological structures in general terms [56]. The SBA was calculated based on the gravity disturbance from each data and Bouguer plate correction using a mean density of 2.67 g/cm^3 [57].

The GGMplus processing blended the GOCE and GRACE data with the EGM 2008 surface gravity data using a full normal equation [20], as expressed in Equation (5). The EGM 2008 is treated as a set of predetermined constants fed into a least-squares algorithm.

$$\left(w_1 N_{sat} + w_2 \sum (x_{EGM})^{-1}\right) x = w_1 n_{sat} + w_2 \sum (x_{EGM})^{-1} x_{EGM} \tag{5}$$

in this equation, N_{sat} and n_{sat} are products of the GOCE and GRACE combination and x is the ideally merged collection of SHCs from EGM 2008, GOCE, and GRACE.

The original dataset of GGMplus was extracted and produced four crucial data: gravity disturbance, gravity acceleration, the vertical component of the satellite sensor, and geoid undulation. The SBA was calculated from GGMplus gravity disturbance. Meanwhile, gravity disturbances of GOCE and SGG-UGM-2 data were received from the International Center for Global Gravity Field Models (<http://icgem.gfz-potsdam.de> (accessed on 1 April 2022)) and processed using the GOCE User Toolbox 3.2.0 program to produce the SBA value.

Various filtering techniques have been widely used in gravity interpretation to detecting the boundary in the gravity anomaly generated by geological structures and tectonic activity below the surface. This study used the First Horizontal Derivative (FHD) and Second Vertical Derivative (SVD) methods. FHD is a technique for horizontally determining the density contrast limit by adjusting the anomalous value [58], and it is calculated using Equation (6). The geological structure in the form of a fault is represented by changes in the FHD anomaly, shown by the greatest value on the FHD graph [59].

$$\text{FHD} = \sqrt{\left(\frac{\partial g}{\partial x}\right)^2 + \left(\frac{\partial g}{\partial y}\right)^2} \tag{6}$$

in the equation, $\frac{\partial g}{\partial x}$ is the horizontal derivative of gravity anomaly in x and $\frac{\partial g}{\partial y}$ is the horizontal derivative of gravity anomaly in y .

The SVD emphasizes near-surface effects at the expense of deeper and shallow anomalies with considerable curvature. The size of the curvature is related to the anomaly depth. The larger the curvature size, the shallower the anomalies [60]. The SVD is calculated using the derivative of the Laplace equation:

$$\text{SVD} = -\left(\frac{\partial^2 g}{\partial x^2} + \frac{\partial^2 g}{\partial y^2}\right) \tag{7}$$

Derivative analysis of the gravity anomaly is to expose the shallow bodies and minimize the regional effect and the deeper structures [60]. The FHD and SVD maps were sliced for helping the anomaly contrast's response analysis to indicate the fault's location. Also, the Bouguer anomaly, FHD, and SVD analyses use information on geological background, volcanoes, and faults in the study area to reduce ambiguity.

4. Results

4.1. Coseismic Source Model Based on Teleseismic Data

The fault plane slip distribution is calculated using the inversion result and assuming that the fault plane is a grid. Each grid box represents a subfault with a strike length and a dip width. The value and slip direction of each subfault are different.

The inversion method uses a band-pass filter frequency of 0.064–0.12 Hz based on trial and error with the smallest variance value. To resolve the earthquake’s source characteristics, it is essential to do a point source inversion before performing a finite-fault inversion. The point source inversion results for the Pasaman M 6.1 earthquake (01:39:28 UTC) were strike 136°, dip 74°, and rake −178°. Figure 7 presents the waveform fitting and point source inversion for the Pasaman earthquake. A variance difference of 0.5740 was calculated between the observed and synthetic signals. A desirable variance value is less than 1.0, which reduces the discrepancy between observed and synthetic data.

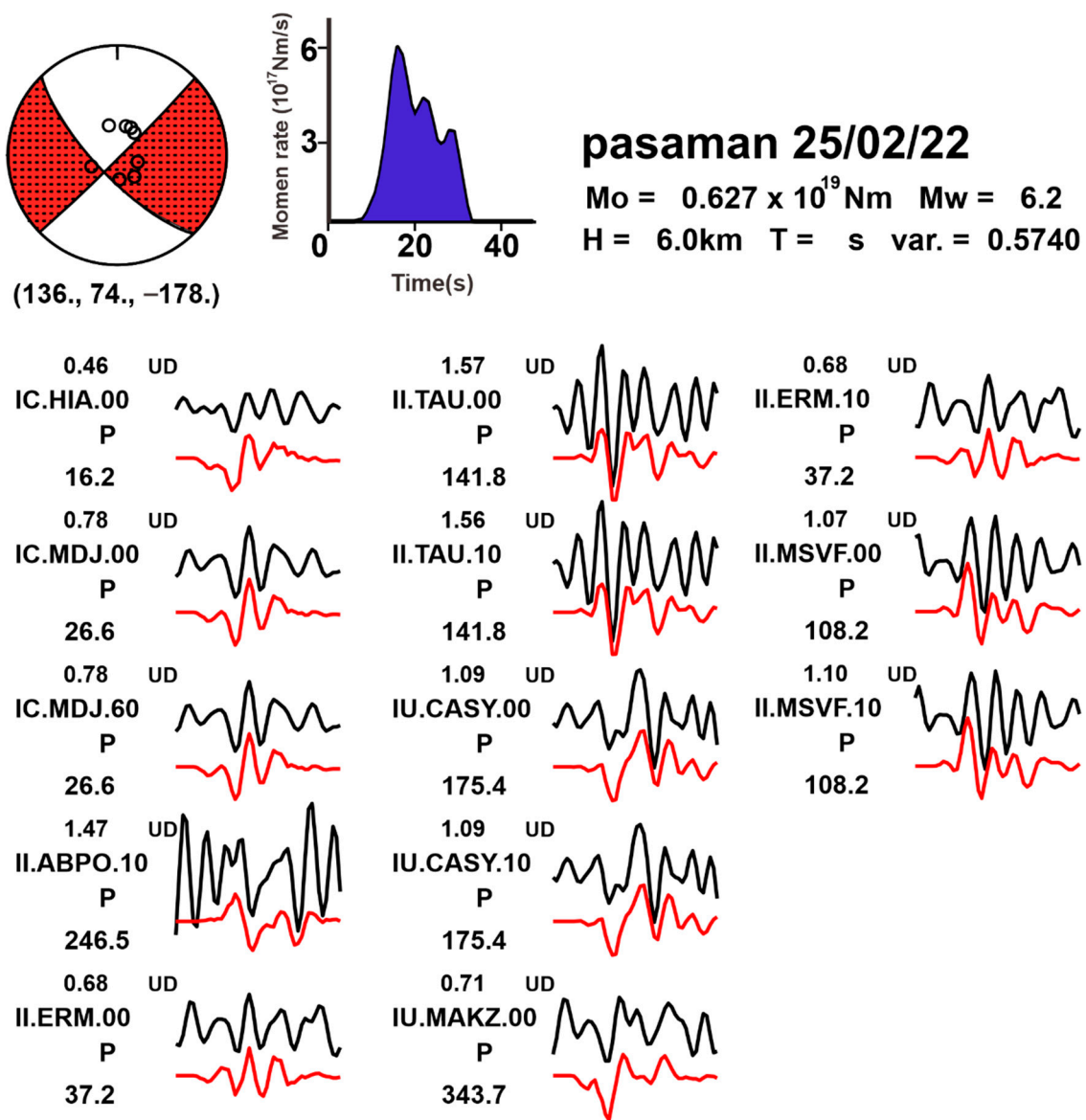
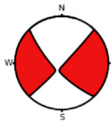
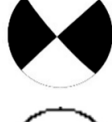
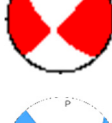
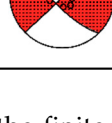


Figure 7. Moment rate function, focal mechanism, and comparison of observation data (black line) and synthesis data (red line) at seismic stations used in the Pasaman earthquake inversion analysis. The small ball on focal mechanism shows the number of recorded seismic stations, red for the compression zone and white for the dilation zone.

A seismic moment M_0 of 0.627×10^{19} Nm is calculated, which updates the magnitude of the moment by Mw 6.2. As shown in the inversion analysis, the fault seems to be a strike-slip fault using a source time of 36 s. Teleseismic body wave inversion produces identical results to those achieved by several associated organizations. A comparison of the focal mechanism results with the other agencies is listed in Table 1. Apart from the outcomes of waveform fits, these results can be used to determine whether the study modeling results are correct.

Table 1. Comparison of the focal mechanism outcomes between this work and various agencies.

No	Agency	Source Parameter			Focal Mechanism	Fault Type
		Strike	Dip	Rake		
1	IRIS	136°	70°	174°		Strike-Slip
2	GFZ	133°	76°	175°		Strike-Slip
3	BMKG	132°	89°	174°		Strike-Slip
4	CMT	136°	70°	174°		Strike-Slip
5	USGS	139°	88°	155°		Strike-Slip
6	This Study	136°	74°	178°		Strike-Slip

After establishing the source, the data are used in the finite-fault inversion. The slip points are assumed to be spatially relative to the fault plane. Figure 8 shows the two-dimensional (2D) spatial distribution of the Pasaman earthquake displacement. The inversion fault plane is predicted to be 24 km-long in the strike direction and 10 km broad in the dip direction. In the strike-and-dip directions, the fault region is split into 12×5 subfault grid boxes of $2 \text{ km} \times 2 \text{ km}$ dimensions each. The initial break is at 0 km strike direction and 0 km dip direction, indicating the location of the hypocenter (red star).

The asperity zone is indicated by the contour size and the length of the slip direction, of which the largest is at 16 km strike direction and 0 km dip direction. The hypocenter is not in the largest asperity zone. A large asperity zone indicates a locked area with a significant possibility of releasing energy. From Figure 8, the greatest energy released is at 16 km in the strike direction and 0 km in the dip direction. The 2D inversion results are then projected using orthogonal projections so that they can spatially map the results. The fault's length and breadth in kilometers are translated to degrees, and the resulting length and width are projected to the surface. This projection guarantees the even distribution of the slip throughout the surface, as shown in Figure 9.

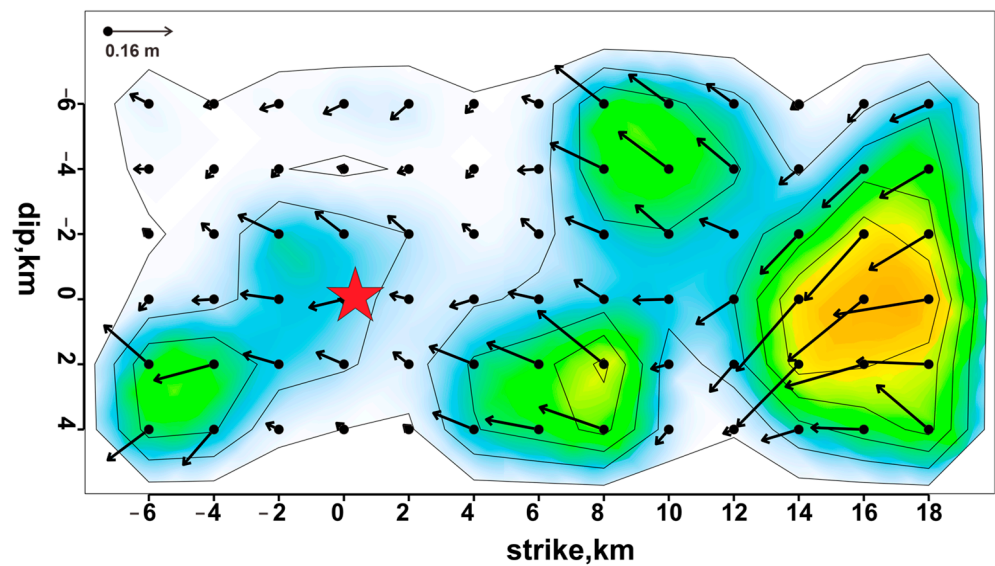


Figure 8. 2D spatial slip distribution of the inversion results (arrows indicate the direction of the slip distribution, and the magnitude indicates the magnitude of the displacement). The color from green to dark yellow means the increase of energy release by the Pasaman earthquake.

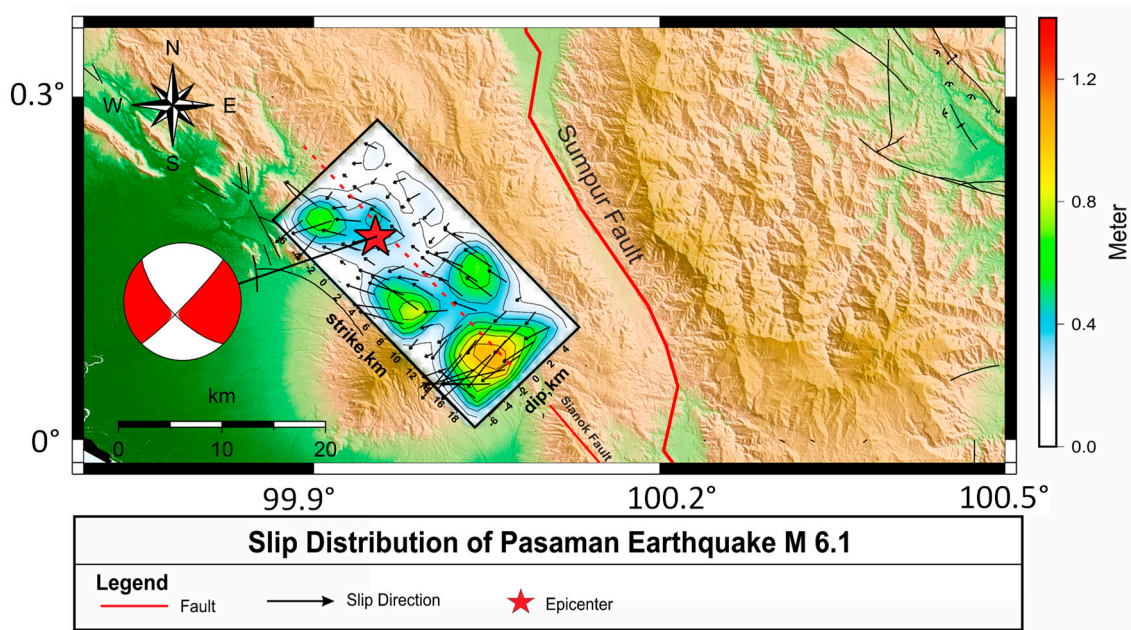


Figure 9. Finite-fault model of teleseismic body wave inversion. The red star represents the epicenter ($M = 6.1$). The red line represents fault segments, while the dashed red line represents the possibility of fault segments generating earthquakes with a strike-slip mechanism.

The results reveal that the greatest slip at the source is 1.01 m. The slip vector is downward in the slip distribution, with the biggest slip in the largest asperity zone. The hypocenter is the point or line in the lithosphere where an earthquake occurs. In Figure 9, the asperity is to the southeast of the earthquake hypocenter on the down-dip section. The fault’s plane’s first rupture occurs at the initial break (or the hypocenter). The most significant energy release of an earthquake occurs in the area of greatest asperity, not in the first rupture of the earthquake [61].

The biggest asperity in the location of the inverted fault is not in the first break. Hence, the maximum energy release occurs to the southeast of the original breach at the fault area’s highest asperity. In the strike direction, the asperity forms as a single in the range of

6–18 km. There is an asperity on the subfault –4 km on strike and 2 km-long in the initial break, but it is not as significant as the asperity that forms on the southeast of the original break. Aside from the fact that this earthquake is a shallow crustal earthquake, the asperity that forms is also a single asperity with the potential to cause significant surface shaking. As demonstrated by the slip distribution's direction leading to a down-dip, the strike-slip source mechanism in the Pasaman earthquake has a slight downhill motion. The asperity distribution is closely related to the magnitude of earthquakes and seismicity patterns in each region [62].

4.2. Fault Detection from Satellite Gravity Data

4.2.1. Simple Bouguer Anomaly (SBA)

Figure 10a–c shows the SBA derived from processing GGMplus, GOCE, and SGG-UGM-2 gravity disturbance data. GGMplus SBA values are in the range of –105 to 35 mGal, whereas GOCE and SGG-UGM SBA anomaly values are in the range of –90 to 70 mGal and –80 to 145 mGal, respectively. The three SBA results share the same color spectrum, from red to blue, corresponding to high- to low-density values. SBA SGG-UGM-2 displays a distinct anomaly pattern from SBA GGMplus and GOCE. For example, in Mount Marapi, the SGG-UGM-2 has a high anomaly value (about 100 mGal), but SBA GGMplus and GOCE have a low anomaly value (around –85 mGal). Because the SGG-UGM-2 has high geographical resolution compared to the other two satellite gravity data, more accurate estimates of anomalies in mountainous and volcanic areas are possible.

Sediment (Pliocene–Eocene and Holocene–Pleistocene) and East Sumatra Block (Lower Permian) dominate the northeastern region. In this region, the anomaly values in the SBA GGMplus, GOCE SBA, and SBA SGG-UGM-2 maps are 5 to 30, 10 to 60, and –5 to 35 mGal, respectively. In the southwest region, the values shown by SBA GGMplus, GOCE, and SGG-UGM-2 are –10 to 25, 10 to 35, and –35 to 10 mGal, respectively. Sediments (Holocene–Pleistocene) comprise the southwest part. This shows that the southwest has a lower average value of anomalies than the northeast. The part is produced by the Young Sedimentary Rock (Holocene–Pleistocene) located near the coastline. By contrast, the sediments (Pliocene–Eocene and Holocene–Pleistocene) and East Sumatra Block generally have higher density values and are located at a higher elevation.

A low anomaly value with a straightness pattern on the SBA map can give a rough estimation of the GSF position. However, the GSF that is shown by the straightness pattern is located in the high value of the anomaly contrast, confirmed by the geological data from the Pasaman region. In Figure 10, the Barumun, Sumpur, and Sianok segments can be discovered in the GGMplus, GOCE, and SGG-UGM-2 SBA contrast anomalies. On the other hand, the Angkola and possible Talamau segments are only discernible in the contrast anomaly observed on the GGMplus. The Barumun, Sumpur, and Sianok segments have large anomalous contrast values compared to the Angkola and possible Talamau segments. This is attributable to the fact that the Barumun, Sumpur, and Sianok segments are the main segments of the GSF. Meanwhile, the Angkola segment is a branch from the Northern Barumun segment, so the anomaly contrast becomes lower and splits, and the Talamau segment is predicted as an extension from Angkola to Sianok segments, shown by low anomaly contrast straightness. We found that the SBA GGMplus, GOCE, and SGG-UGM-2 can clearly identify the locations of the main segments of the GSF, as shown by a high anomaly contrast between them. In addition, GGMplus is also more sensitive, so it is able to detect the existence of a fault segment with a low contrast anomaly compared to that presented for the Angkola and Talamau segments.

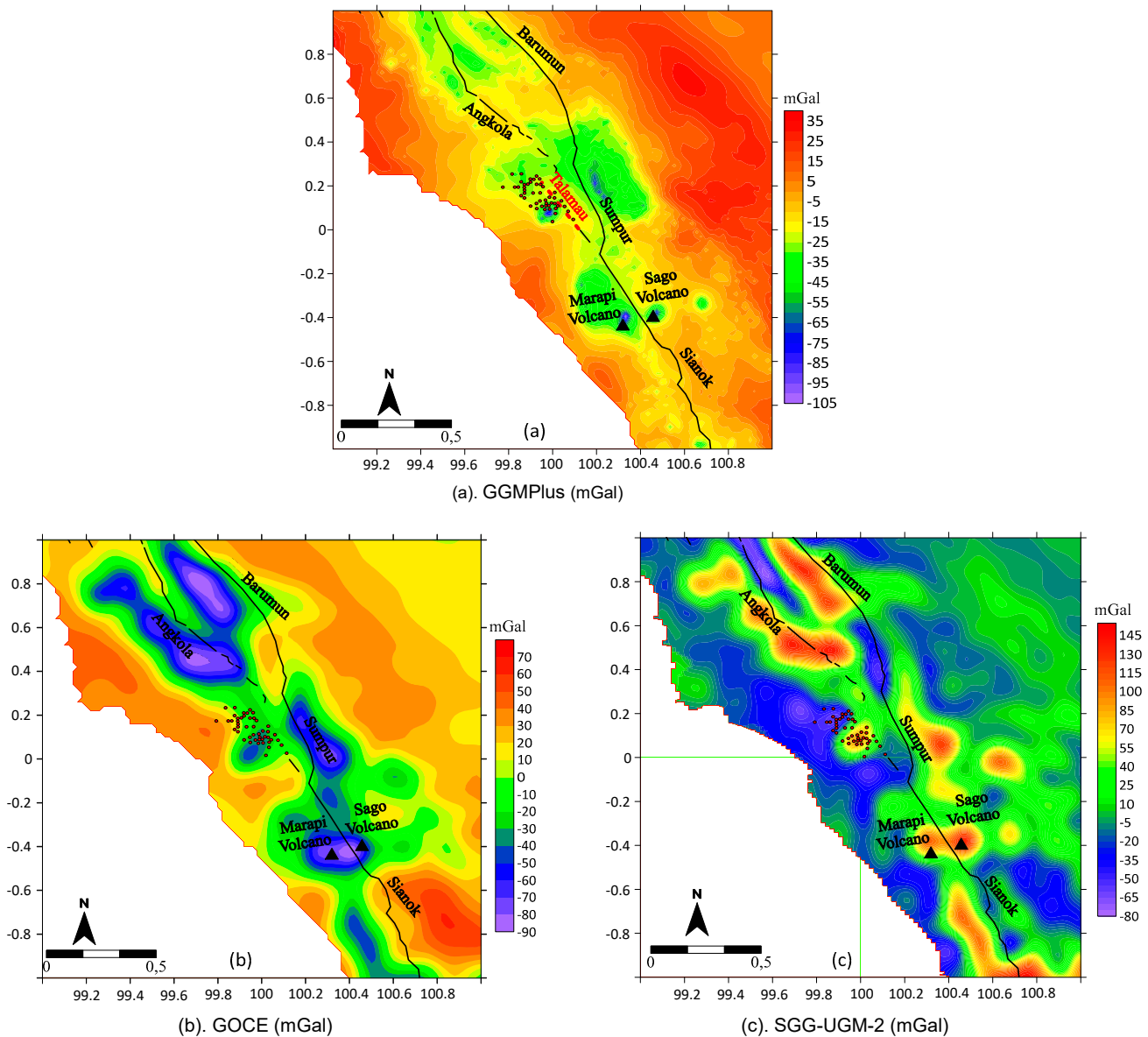


Figure 10. (a) GGMplus SBA, (b) GOCE SBA, and (c) SGG-UGM-2 SBA. Faults are symbolized by a black straight line, volcanoes are represented by a black triangle, a red dotted line symbolizes the inferred Talamau fault, and red dots illustrates aftershocks distribution.

About the 2022 Pasaman earthquake, aftershock distribution can be used as evidence for this earthquake not generated by the Barumun, Angkola, Sumpur, and Sianok segments, which are more accurately defined as active fault segments. However, it is more likely generated by the Talamau fault, which has been inactive for an extended period. The aftershock distribution took place in the same place as the anomalous contrast of the Talamau fault segment. Nevertheless, fault location prediction from the SBA still has residual and regional abnormalities; hence, it is important to filter it through the analysis of the FHD and SVD to get a clear picture of the fault pattern (SVD).

4.2.2. Data Transformation

Figure 11a shows the FHD gravity anomaly of GGMplus in the range of 0–160 mGal. Several places, such as the Marapi Volcano, the Sago Volcano, the border between Lake Maninjau and the land around it, the Volcanic Formations, and the West Sumatra Block,

are shown with high anomalous zones. On the other hand, the GSF, in the FHD anomaly, shows a low anomaly pattern, which extends from north to south, ranging from 0–25 mGal.

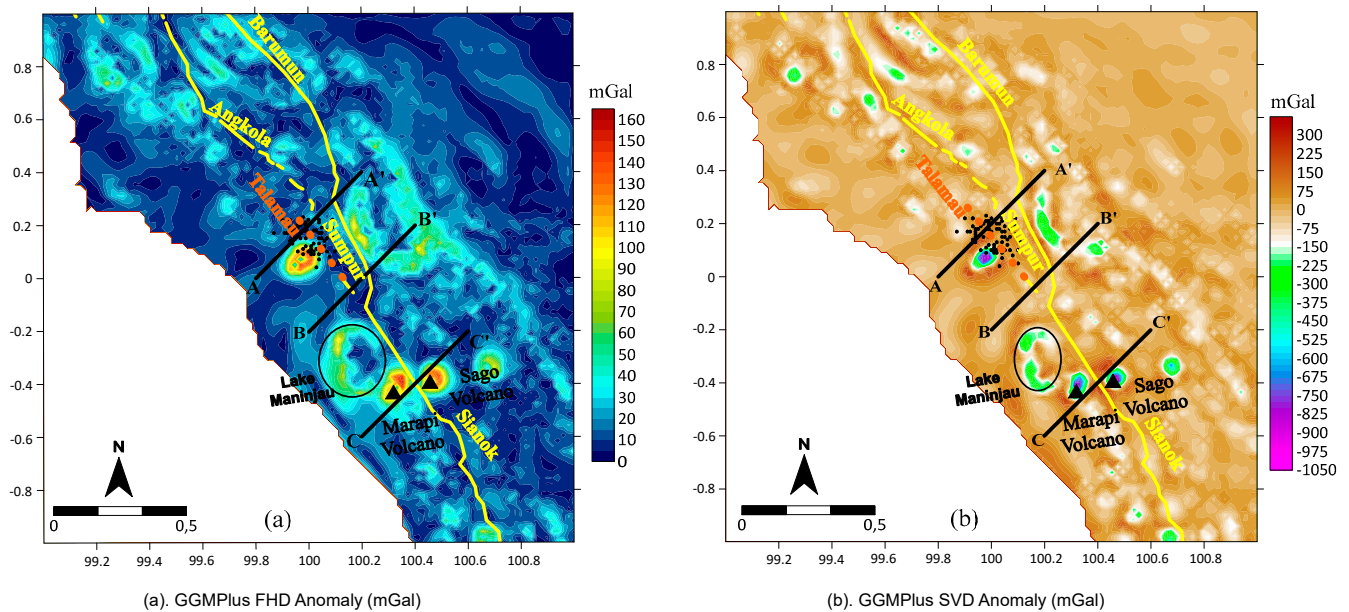


Figure 11. (a) FHD anomaly and (b) SVD anomaly. Faults are symbolized by a black straight line, volcanoes are represented by a black triangle, the alleged Talamau fault is symbolized by a orange dotted line, Lake Singkarak is symbolized by a blue ellipse, and slicing is symbolized by a black straight line.

As shown in Figure 11b presents the GGMPplus SVD gravity anomaly in the range of -1050 to 350 mGal. In contrast to the FHD, the Marapi Volcano, Sago Volcano, Lake Maninjau border, and nearby areas indicate low SVD anomaly values. The SVD analysis shows that there is a zero-value anomaly near the boundary between the West Sumatra Block and Volcanics Formations and in the GSF.

To better understand the location of the segment faults, a cross-sectional analysis of the FHD and SVD data was performed, shown with AA', BB', and CC' sections, as well as the red box (referring to the predicted existence of the Talamau segment) and black box (the location of the GSF in the Pasaman region, consisting of the Barumun, Sumpur, and Sianok segments) (Figure 12).

The AA' and BB' slices are positioned perpendicular to the supposed Talamau segment until they cross through the Sumpur segment as part of the GSF. In the red box, the estimated area of the Talamau segment on slice AA' is about $0.3\text{--}0.33^\circ$ away, with a maximum FHD anomaly value of approximately 25 mGal. For the slice BB', it is nearly $0.21\text{--}0.24^\circ$ away, with a maximum value of nearly 15 mGal. On the other hand, in the black box, the slice AA' is placed at a distance of $0.4\text{--}0.44^\circ$ with a maximum anomaly value of ~ 16 mGal. The slice BB' is positioned at a distance of $0.28\text{--}0.33^\circ$ with a maximum anomaly value of approximately 14 mGal. The slice CC' is perpendicular to the Sianok segment. The black box slice CC' defines the region indicating the presence of the Sianok segment, which is $0.28\text{--}0.34^\circ$ away and has a maximum value of approximately 85 mGal, as it is located between two volcanoes. The segment distance between Sianok on the CC' slice and Sumpur on the BB' slice is nearly identical. The cross-section shows that the slice with the highest FHD value shows a geological feature in the form of a fault segment.

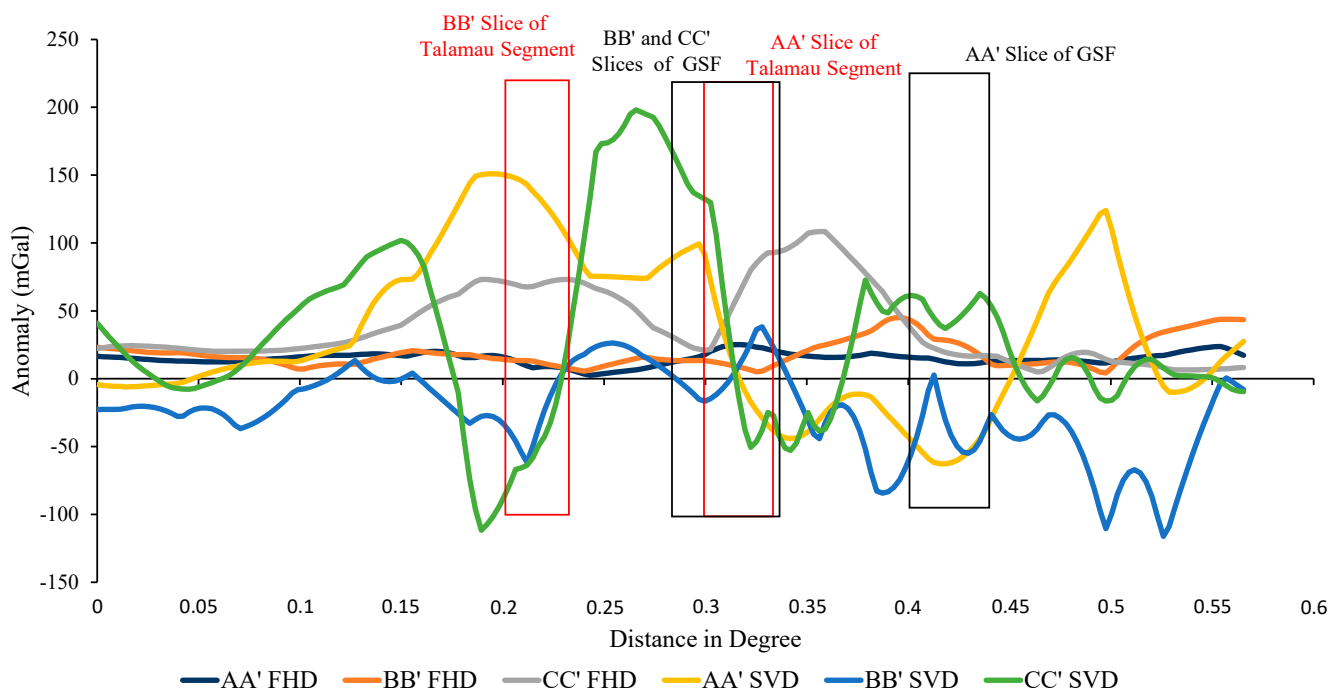


Figure 12. Results of AA' FHD, BB' FHD, CC' FHD, AA' SVD, BB' SVD, and CC' SVD is symbolized by dark blue, orange, gray, yellow, blue, and green lines. Red rectangles show the new fault segment, the Talamau segment, while the black rectangles show the old segment.

The analysis of the SVD value reveals that the fault segment indicator is on the low anomaly graph with a curvature of less than 0 mGal. The SVD values demonstrate it in slices AA' and BB', which are around -10 and -60 mGal in the region of the supposed Talamau segment (red box). However, in the Sumpur segment, slice AA' has an SVD value of around -60 mGal, while slice BB' has a value of approximately -20 mGal. The detection of Talamau and Sumpur segments in the SVD analysis corresponds to the same region as the FHD analysis, as indicated by the AA' slice between 0.33° and 0.33° and the BB' slice between 0.21° and 0.21° . In the Sianok segment (black box), the CC' slice has an SVD value of -50 mGal at the same distance as the CC' FHD slice, which is between 0.28° and 0.34° .

SVD analysis can also be seen in terms of curvature size. This study focuses on Talamau, Sumpur, and Sianok for curvature investigation. In the Talamau and Sumpur segments, AA's slice curvature is larger than BB's. The Talamau and Sumpur segments on the AA' slice are located at a shallow depth compared to those on the BB' slice. In addition, the CC' slice of the Sianok segment has a small curvature compared to the BB' slice of the Talamau segment. By contrast, the curvature of the CC' Sianok segment is small when compared to the BB' Sumpur segment slice. When the Sianok segment is compared to the Talamau and Sumpur segments, it is clear that the Sianok segment is the deepest.

5. Discussion

The Pasaman area has four main active fault segments, namely, Barumun, Angkola, Sumpur, and Sianok. Moreover, there is also a Talamau segment that is categorized as an uncertain fault by the Geological Map produced by Rock, N. M. S. et al. (1983) [40]. The slip rates of fault segments covering the Pasaman are 23 ± 4 mm/y [7]. The Sumatra subduction zone is responsible for the high slip rate in the Pasaman area, including the activities of the Barumun, Angkola, Sianok, and Sumpur segments. Because of such complex tectonic conditions, the Pasaman area experienced earthquakes in 1977 and 2022. The 1977 earthquake (magnitude 6.1) occurred near the Angkola segment [63], while the 2022 earthquake (magnitude 6.2) was in close proximity to the Sianok, Sumpur, and

Angkola segment faults. On the other hand, the BMKG catalog shows that the Talamau uncertain fault did not have any seismic activity before the 2022 Pasaman earthquake.

It is interesting that, from the teleseismic result, the 2022 earthquake in Pasaman originated from an uncertain fault segment, that is, the Talamau segment. We tried to compare our source parameter result with the other institutions. From Table 1, the source parameter, which is produced in this study (strike: 136° ; dip: 74° ; rake: 178°) is slightly different from the other institutions, such as IRIS (strike: 136° ; dip: 70° ; rake: 174°), GFZ (strike: 133° ; dip: 76° ; rake: 175°), BMKG (strike: 132° ; dip: 89° ; rake: 174°), CMT (strike: 136° ; dip: 70° ; rake: 174°), and USGS (strike: 139° ; dip: 88° ; rake: 155°). According to the teleseismic inversion and its asperity zone, the 2022 Pasaman earthquake originating from the Sianok fault segment was pushed to the north and reached the uncertain fault segment in the Talamau area. As evidenced by the asperity caused by the M 6.2 Pasaman earthquake, the southeastern region of the hypocenter has a single major asperity. These results imply that the fragile area [64] is responsible for activating the Talamau segment.

The SBA GGMplus satellite gravity data could explain the existence of the Talamau fault segment. This technique was used to detect the GSF fault location in Aceh Province [26]. To ensure the existence of the Talamau fault segment, we also used the FHD and SVD methods [60] and then analyzed the pattern. Using the pattern and the cross-section analysis of the GGMplus FHD and SVD, the Talamau fault segment becomes more clear. Also, the curvature size from the SVD cross-sections also shows the depth of each segment in the Pasaman area, which exposes the Sianok segment as the deepest segment compared to the Talamau and Sumpur segments.

6. Conclusions

From the results, it can be concluded that a combined teleseismic and gravity observation methodology is potentially useful for delineating the fault structure that caused the 2022 Pasaman earthquake. The combination of these two methods can mutually reinforce the findings of coseismic deformation from the event. Based on the teleseismic inversion data, the type of fault is strike-slip with a slight decrease and a source period of 36 s and the magnitude of this earthquake was 6.2.

The hypocenter is not in the maximum asperity zone, which is located at 16 km in the dip direction and 0 km in the strike direction from the hypocenter. The length of the line shows it from the slip point, with its size reaching 1.01 m. The major asperity in the inverted fault's position is not in the initial break. As a result, the most significant energy release occurs near the fault area's highest asperity, which is located in the southern part of the original break. According to the teleseismic inversion results, the coseismic deformation of the 2022 Pasaman earthquake was generated by regional tectonism, which was localized along the Sianok fault and then spread to the north and reached the uncertain fault segment in the Talamau area.

The Talamau segment could be detected from SBA maps (still including the regional effect) from the GGMplus data, which overlapped with the aftershock distribution. The SBA GGMplus has a stronger pattern than the SBA from the GOCE and SGG-UGM-2 satellite gravity data. After the regional effect was deleted using the FHD and SVD analysis, the straightness pattern of the Talamau faults was clearer. Also, the cross-section analysis of FHD and SVD from the GGMplus analysis confirmed the existence of the Talamau segment fault.

Author Contributions: Conceptualization, B.G.D., L.S.H. and R.P.; methodology, B.G.D. and R.P.; software, A.S.N.; validation, B.G.D., I.S. and A.M.J.; formal analysis, B.G.D., R.P., I.S., A.S.N. and M.Y.; investigation, L.S.H., I.S. and B.G.D.; resources, A.M.J., M.Y. and L.S.H.; data curation, A.S.N. and R.P.; writing—original draft preparation, B.G.D., R.P., M.Y. and A.S.N.; writing—review and editing, L.S.H., B.G.D., I.S., M.Y. and A.M.J.; visualization, M.Y., B.G.D., A.S.N. and R.P.; supervision, L.S.H., B.G.D., I.S. and A.M.J. All authors have read and agreed to the published version of the manuscript.

Funding: This research received no external funding.

Institutional Review Board Statement: Not applicable.

Informed Consent Statement: Not applicable.

Data Availability Statement: GGMPlus data can be found here: http://ddfe.curtin.edu.au/gravity_models/GGMplus/ (accessed on 1 April 2022). Teleseismic data can be obtained on request from: https://ds.iris.edu/wilber3/find_event (accessed on 8 April 2022). Seismic data can be obtained from the Soil properties data can be obtained on request from the Earthquake and Tsunami Center, Agency for Meteorology Climatology and Geophysics (BMKG).

Acknowledgments: The author would like to thank the Geodesy, Geometry and Physical Geodesy (GGGF) laboratory, Department of Geodetic Engineering, Universitas Gadjah Mada, for technical support. We also appreciate the Earthquake and Tsunami Center, Agency for Meteorology Climatology and Geophysics (BMKG), for providing their data at the study area for analysis. Most figures were generated by the Generic Mapping Tools [65] and QGIS [66].

Conflicts of Interest: The authors declare no conflict of interest.

References

- Bellier, O.; Sébrier, M.; Pramumijoyo, S.; Beaudouin, T.; Harjono, H.; Bahar, I.; Forni, O. Paleoseismicity and Seismic Hazard Along the Great Sumatran Fault (Indonesia). *J. Geod.* **1997**, *24*, 169–183. [CrossRef]
- Noda, A. Strike-Slip Basin—Its Configuration and Sedimentary Facies. In *Mechanism of Sedimentary Basin Formation—Multidisciplinary Approach on Active Plate Margins*; IntechOpen: London, UK, 2013. [CrossRef]
- Natawidjaja, D.H.; Bradley, K.; Daryono, M.R.; Aribowo, S.; Herrin, J. Late Quaternary Eruption of the Ranau Caldera and New Geological Slip Rates of the Sumatran Fault Zone in Southern Sumatra, Indonesia. *Geosci. Lett.* **2017**, *4*, 21. [CrossRef]
- Acocella, V.; Bellier, O.; Sandri, L.; Sébrier, M.; Pramumijoyo, S. Weak Tectono-Magmatic Relationships Along an Obliquely Convergent Plate Boundary: Sumatra, Indonesia. *Front. Earth Sci.* **2018**, *6*, 3. [CrossRef]
- Muraoka, H.; Takahashi, M.; Sundhoro, H.; Dwipa, S.; Soeda, Y.; Momita, M.; Shimada, K. Geothermal Systems Constrained by the Sumatran Fault and Its Pull-Apart Basins in Sumatra, Western Indonesia. In Proceedings of the World Geothermal Congress 2010, Bali, Indonesia, 25–30 April 2010.
- Aydin, A.; Nur, A. Evolution of Pull-Apart Basins and Their Scale Independence. *Tectonics* **1982**, *1*, 91–105. [CrossRef]
- Natawidjaja, D.H.; Triyoso, W. The Sumatran Fault Zone—From Source to Hazard. *J. Earthq. Tsunami* **2007**, *1*, 21–47. [CrossRef]
- Sieh, K.; Natawidjaja, D. Neotectonics of the Sumatran Fault, Indonesia. *J. Geophys. Res.* **2000**, *105*, 28295–28326. [CrossRef]
- Rock, N.M.S.; Aldiss, D.T.; Aspden, J.A.; Clarke, M.C.G.; Djunuddin, A.; Kartawa, W.; Miswar, T.S.J.; Whandoyo, R. *Geologic Map of the Lubuksikaping Quadrangle, Sumatra*; Geological Research and Development Centre: Bandung, Indonesia, 1983.
- Allen, R.M.; Ziv, A. Application of Real-Time GPS to Earthquake Early Warning. *Geophys. Res. Lett.* **2011**, *38*, L16310. [CrossRef]
- Hreinsdóttir, S.; Freymueller, J.T.; Bürgmann, R.; Mitchell, J. Coseismic Deformation of the 2002 Denali Fault Earthquake: Insights from GPS Measurements. *J. Geophys. Res.* **2006**, *111*, B03308. [CrossRef]
- Yamanaka, Y.; Kikuchi, M. Asperity Map Along the Subduction Zone in Northeastern Japan Inferred from Regional Seismic Data. *J. Geophys. Res.* **2004**, *109*, B07307. [CrossRef]
- Murotani, S.; Satake, K.; Fujii, Y. Scaling Relations of Seismic Moment, Rupture Area, Average Slip, and Asperity Size for M~9 Subduction-Zone Earthquakes. *Geophys. Res. Lett.* **2013**, *40*, 5070–5074. [CrossRef]
- Lo, W.; Purnomo, S.N.; Dewanto, B.G.; Sarah, D.; Sumiyanto. Integration of Numerical Models and InSAR Techniques to Assess Land Subsidence Due to Excessive Groundwater Abstraction in the Coastal and Lowland Regions of Semarang City. *Water* **2022**, *14*, 201. [CrossRef]
- Dewanto, B.G.; Haryanto, Y.; Purnomo, S.N. Land Subsidence Potential Detection in Yogyakarta International Airport Using Sentinel-1 InSAR Data. *Civ. Eng. Dimens.* **2021**, *23*, 91–99. [CrossRef]
- Kikuchi, M.; Nakamura, M.; Yoshikawa, K. Source Rupture Processes of the 1944 Tonankai Earthquake and the 1945 Mikawa Earthquake Derived from Low-Gain Seismograms. *Earth Planet Sp.* **2003**, *55*, 159–172. [CrossRef]
- Sandwell, D.T.; Smith, W.H.F. Marine Gravity Anomaly from Geosat and ERS 1 Satellite Altimetry. *J. Geophys. Res.* **1997**, *102*, 10039–10054. [CrossRef]
- Kern, M.; Schwarz, K.P.; Sneeuw, N. A Study on the Combination of Satellite, Airborne, and Terrestrial Gravity Data. *J. Geod.* **2003**, *77*, 217–225. [CrossRef]
- Zhang, Y.-Z.; Xu, H.-J.; Wang, W.-D.; Duan, H.-R.; Zhang, B.-P. Gravity Anomaly from Satellite Gravity Gradiometry Data by GOCE in Japan Ms 9.0 Strong Earthquake Region. *Procedia Environ. Sci.* **2011**, *10*, 529–534. [CrossRef]
- Hirt, C.; Claessens, S.; Fecher, T.; Kuhn, M.; Pail, R.; Rexer, M. New Ultrahigh-Resolution Picture of Earth's Gravity Field. *Geophys. Res. Lett.* **2013**, *40*, 4279–4283. [CrossRef]
- Hirt, C. Prediction of Vertical Deflections from High-Degree Spherical Harmonic Synthesis and Residual Terrain Model Data. *J. Geod.* **2010**, *84*, 179–190. [CrossRef]
- Hirt, C.; Kuhn, M.; Claessens, S.; Pail, R.; Seitz, K.; Gruber, T. Study of the Earth's Short-Scale Gravity Field Using the ERTM2160 Gravity Model. *Geosci. Comput.* **2014**, *73*, 71–80. [CrossRef]

23. Wada, S.; Sawada, A.; Hiramatsu, Y.; Matsumoto, N.; Okada, S.; Tanaka, T.; Honda, R. Continuity of Subsurface Fault Structure Revealed by Gravity Anomaly: The Eastern Boundary Fault Zone of the Niigata Plain, Central Japan. *Earth Planets Sp.* **2017**, *69*, 15. [[CrossRef](#)]
24. Riedel, S.; Jokat, W.; Steinhage, D. Mapping Tectonic Provinces with Airborne Gravity and Radar Data in Dronning Maud Land, East Antarctica. *Geophys. J. Int.* **2012**, *189*, 414–427. [[CrossRef](#)]
25. Hiramatsu, Y.; Sawada, A.; Kobayashi, W.; Ishida, S.; Hamada, M. Gravity Gradient Tensor Analysis to an Active Fault: A Case Study at the Togi-Gawa Nangan Fault, Noto Peninsula, Central Japan. *Earth Planets Sp.* **2019**, *71*, 107. [[CrossRef](#)]
26. Yanis, M.; Abdullah, F.; Zaini, N.; Ismail, N. The Northernmost Part of the Great Sumatran Fault Map and Images Derived from Gravity Anomaly. *Acta Geophys.* **2021**, *69*, 795–807. [[CrossRef](#)]
27. Julius, A.M.; Pribadi, S.; Saputra, A.A.; Prayitno, B.S.; Ahadi, S.; Hermanto, D.; Arifin, H.; Satria, L.A.; Zevanya, C.S.S. An On-Site Post-Event Survey of the 2022 Mw 6.1 Western Pasaman Sumatera Destructive Earthquake. *NTU J. Renew. Energy* **2022**, *2*, 39–49.
28. Kardo, R.; Mulyani, R.R.; Yulastri, W. Play Therapy as a Trauma Healing Effort in Children Victims of the Earthquake in Nagari Pasaman. *J. Community Public Serv.* **2022**, *1*, 90–94.
29. Irkani, P.; Antomi, Y.; Yulfa, A.; Purwaningsih, E.; Triyatno. Visualisasi Potensi Daerah Kabupaten Pasaman Barat dalam Format Multimedia. 2010. Available online: repository.unp.ac.id/5919/1/PAUS%20ISKARNI_546_10.pdf (accessed on 5 April 2022).
30. Iskarni, P.; Antomi, Y.; Yulfa, A.; Purwaningsih, E.; Triyatno. *Visualization of the Potential of West Pasaman Regency in Multi Media Format*; Regional Development Planning Agency, West Pasaman Regency Government in Collaboration with the Padang State University Spatial Data Infrastructure Development Center: Padang, Indonesia, 2010.
31. Hall, R. Late Jurassic–Cenozoic Reconstructions of The Indonesian Region and The Indian Ocean. *Tectonophysics* **2012**, 570–571, 1–41. [[CrossRef](#)]
32. Barber, A.J.; Crow, M.J. Structure of Sumatra and its Implications for the Tectonic Assembly of Southeast Asia and the Destruction of Paleotethys. *Island Arc.* **2009**, *18*, 3–20. [[CrossRef](#)]
33. Ghosal, D.; Singh, S.C.; Chauhan, A.P.S.; Hananto, N.D. New Insights on the Offshore Extension of the Great Sumatran Fault, NW Sumatra, from Marine Geophysical Studies. *Geochem. Geophys. Geosyst.* **2012**, *13*, Q0AF06. [[CrossRef](#)]
34. De Maisonneuve, C.B.; Bergal-Kuvikas, O. Timing, Magnitude and Geochemistry of Major Southeast Asian Volcanic Eruptions: Identifying Tephrochronologic Markers. *J. Quat. Sci.* **2020**, *35*, 272–287. [[CrossRef](#)]
35. Chesner, C.A.; Rose, W.I. Stratigraphy of the Toba Tuffs and the Evolution of the Toba Caldera Complex, Sumatra, Indonesia. *Bull. Volcanol.* **1991**, *53*, 343–356. [[CrossRef](#)]
36. Chesner, C.A. The Toba Caldera Complex. *Quat. Int.* **2012**, *258*, 5–18. [[CrossRef](#)]
37. Pearce, N.J.G.; Westgate, J.A.; Gatti, E.; Pattan, J.N.; Parthiban, G.; Achyuthan, H. Individual Glass Shard Trace Element Analyses Confirm that All Known Toba Tephra Reported from India is from The C 75-Ka Youngest Toba Eruption. *J. Quat. Sci.* **2014**, *29*, 729–734. [[CrossRef](#)]
38. Purbo-Hadiwidjojo, M.M.; Sjahrudin, M.L.; Suparka, S. The volcano-tectonic history of the Maninjau Caldera, Western Sumatra, Indonesia. Fixism, mobilism or relativism: Van Bemmelen’s search for harmony. *Geol. Mijnb.* **1979**, *58*, 193–200.
39. Brent, V.A.; Agung, P.; John, A.W.; Michael, B.; Keith, F.; Alan, H.; Ian, S. Correspondence Between Glass-FT and ¹⁴C Ages of Silicic Pyroclastic Flow Deposits Sourced from Maninjau Caldera, West-Central Sumatra. *Earth Planet. Sci. Lett.* **2004**, *227*, 121–133. [[CrossRef](#)]
40. Indranova, S.; Atsushi, T.; Agung, H.; Haryo, E.W. The Origins of Transparent and Non-Transparent White Pumice: A Case Study of the 52 Ka Maninjau Caldera-Forming Eruption, Indonesia. *J. Volcanol. Geotherm.* **2022**, *431*, 107643. [[CrossRef](#)]
41. Zulkarnain, I.; Indarto, S.; Sudarsono, S.I. Geochemical Signatures of Volcanic Rocks Related to Gold Mineralization: A Case of Volcanic Rocks in Pasaman Area, West Sumatra, Indonesia. *RISSET-Geol. Pertamb.* **2005**, *15*, 1. [[CrossRef](#)]
42. Wald, D.J.; Heaton, T.H. Spatial and Temporal Distribution of Slip for the 1992 Landers, California, Earthquake. *Bull. Seism. Soc. Am.* **1994**, *84*, 668–691. [[CrossRef](#)]
43. Ide, S.; Takeo, M.; Yoshida, Y. Source Process of the 1995 Kobe Earthquake: Determination of Spatio-Temporal Slip Distribution by Bayesian Modeling. *Bull. Seism. Soc. Am.* **1996**, *86*, 547–566. [[CrossRef](#)]
44. Kikuchi, M.; Kanamori, H.; Satake, K. Source Complexity of the 1988 Armenian Earthquake: Evidence for a Slow After-Slip Event. *J. Geophys. Res. Solid Earth* **1993**, *98*, 15797–15808. [[CrossRef](#)]
45. Pacheco, J.F.; Estabrook, C.H.; Simpson, D.W.; Nabelek, J. Teleseismic Body Wave Analysis of the 1988 Armenian Earthquake. *Geophys. Res. Lett.* **1989**, *16*, 1425–1428. [[CrossRef](#)]
46. Jeffreys, H.; Bullen, K.E. *Seismological Tables*; Office of the British Association, Burlington House: London, UK, 1958.
47. Bouchon, M. Teleseismic Body Wave Radiation from a Seismic Source in a Layered Medium. *Geophys. J. R. Astron. Soc.* **1976**, *47*, 515–530. [[CrossRef](#)]
48. Haskell, N.A. Crustal Reflection of Plane SH Waves. *J. Geophys. Res.* **1960**, *65*, 4147–4150. [[CrossRef](#)]
49. Haskell, N.A. Crustal Reflection of Plane P and SV Waves. *J. Geophys. Res.* **1962**, *67*, 4751–4767. [[CrossRef](#)]
50. Novak, P.; Heck, B. Downward Continuation and Geoid Determination Based on Band-Limited Airborne Gravity Data. *J. Geod.* **2002**, *76*, 269–278. [[CrossRef](#)]
51. Keating, P.; Pinet, N. Comparison of Surface and Shipborne Gravity Data with Satellite-Altitude Gravity Data in Hudson Bay. *Lead. Edge* **2013**, *32*, 450–458. [[CrossRef](#)]

52. Ma, G.; Gao, T.; Li, L.; Wang, T.; Niu, R.; Li, X. High-Resolution Cooperate Density-Integrated Inversion Method of Airborne Gravity and Its Gradient Data. *Remote Sens.* **2021**, *13*, 4157. [[CrossRef](#)]
53. Sandwell, D.T.; Smith, W.H.F. Global Marine Gravity from Retracked Geosat and ERS-1 Altimetry: Ridge Segmentation Versus Spreading Rate. *J. Geophys. Res. Solid Earth* **2009**, *114*, B01411. [[CrossRef](#)]
54. Kirschner, M.; Massmann, F.H.; Steinhoff, M.; GRACE. *Distributed Space Missions for Earth System Monitoring*; Springer: New York, NY, USA, 2013. [[CrossRef](#)]
55. Gruber, T.; Visser, P.N.A.M.; Ackermann, C.; Hosse, M. Validation of GOCE Gravity Field Models by Means of Orbit Residuals and Geoid Comparisons. *J. Geod.* **2011**, *85*, 845–860. [[CrossRef](#)]
56. Wang, X.; Jiang, W.; Zhang, J.; Shen, W.; Fu, Z. Gravity Anomaly and Fine Crustal Structure in The Middle Segment of the Tan-Lu Fault Zone, Eastern Chinese Mainland. *J. Asian Earth Sci.* **2022**, *224*, 105027. [[CrossRef](#)]
57. Tassis, G.A.; Grigoriadis, V.N.; Tziavos, I.N.; Tsokas, G.N.; Papazachos, C.B.; Vasiljević, I. A New Bouguer Gravity Anomaly Field for the Adriatic Sea and its Application for the Study of the Crustal and Upper Mantle Structure. *J. Geodyn.* **2013**, *66*, 38–52. [[CrossRef](#)]
58. Telford, W.M.; Geldart, L.P.; Sheriff, R.E. *Applied Geophysics*; Cambridge University Press: Cambridge, UK, 1990. [[CrossRef](#)]
59. Reynolds, J.M. *An Introduction to Applied and Environmental Geophysics*; John Wiley & Sons: Hoboken, NJ, USA, 1997; ISBN 978-0-470-97544-2.
60. Pal, S.K.; Majumdar, T.J. Geological Appraisal over the Singhbhum-Orissa Craton, India using GOCE, EIGEN6-C2 and In Situ Gravity Data. *Int. J. Appl. Earth Obs. Geoinfo.* **2015**, *35*, 96–119. [[CrossRef](#)]
61. Kikuchi, M.; Kanamori, H. Inversion of Complex Body Waves—III. *Bull. Seismol. Soc. Am.* **1991**, *81*, 2335–2350. [[CrossRef](#)]
62. Yagi, Y.; Mikumo, T.; Pacheco, J.; Rayes, G. Source Rupture Process of the Tecoman, Colima, Mexico Earthquake of 22 January 2003, Determined by Joint Inversion of Teleseismic Body-Wave and Nearsurface Data. *Bull. Seismol. Soc. Am.* **2004**, *94*, 1795–1807. [[CrossRef](#)]
63. Setiyono, U.; Gunawan, I.; Priyobudi; Yatimantoro; Hidayanti; Anggraini, S.; Rahayu, R.H.; Yogaswara, D.S.; Julius, A.M.; Apriyani, M.; et al. *Catalog of Significant and Destructive Earthquakes 1821–2017*; Earthquake and Tsunami Center, Meteorology, Climatology, and Geophysical Agency of Indonesia (BMKG): Jakarta, Indonesia, 2018; ISBN 2477-0582.
64. Chen, X.; Carpenter, B.M.; Reches, Z. Asperity Failure Control of Stick–Slip along Brittle Faults. *Pure Appl. Geophys.* **2020**, *177*, 3225–3242. [[CrossRef](#)]
65. Wessel, P.; Smith, W.H.F.; Scharroo, R.; Luis, J.; Wobbe, F. Generic Mapping Tools: Improved Version Released. *EOS Trans. AGU* **2013**, *94*, 409–410. [[CrossRef](#)]
66. QGIS Development Team. QGIS Geographic Information System. Open Source Geospatial Foundation Project. 2022. Available online: <http://qgis.osgeo.org> (accessed on 5 April 2022).